



Radionuclides Migration Related to Alteration and Mineralogical Investigations of El Sela Uraniferous Two Mica Granites

Magdy Abdallah ¹, A. M. El-Mezayen ¹, El-Afandy H. Adel ², Ahmed M. El-Shabasy ³, Osama Draz ², Sherif A. Taalab ^{1*}



CrossMark

¹ Geology Department, Faculty of Science, Al-Azhar University, Cairo 11884, Egypt

² Nuclear Materials Authority, P.O. Box 530, El Maadi, Cairo, Egypt

³ Radiation Protection Department, Egyptian Nuclear and Radiological Regulatory Authority (ENRRA), Cairo, Egypt

Abstract

El Sela granites are located 25 kilometers west of Abu Ramad and primarily covered by two-mica granites, muscovite granite, and biotite granite, which intruded by younger types of dikes and veins. The studied granites were measured radiometrically by HPGe-detector and investigated mineralogically by Scan Electron Microscope and X-ray diffraction techniques. This work aims to evaluate the radioelement distribution and study the uranium migration processes in the two mica granites. Uranium contents in these granites are more than twice Clark values confirming their uranium nature. Increments in the chemical index were accompanied by decrements in both uranium and thorium, exhibiting uranium leaching during alteration processes with thorium adsorption on clay minerals. The $^{234}\text{U}/^{235}\text{U}$ and $^{238}\text{U}/^{235}\text{U}$ ARs indicate their shifting positively and/or negatively from the natural ratio, exhibiting the role of the alteration processes in redistribution radioelements. The $^{234}\text{U}/^{238}\text{U}$ ARs is mostly lesser than unity, manifesting ^{234}U migration out in these rocks through the prevailing oxidation-reduction conditions. The plot of $^{234}\text{U}/^{238}\text{U}$ versus $^{230}\text{Th}/^{238}\text{U}$ clarify that the rock samples have been affected by leaching-accumulation events in the period from ($>3 \times 10^4$ to $>6 \times 10^4$ years). Mineralogically, the uraniumiferous granites have uranophane, kasolite, autunite, zircon, apatite, titanite, pyrite and rutile minerals.

Keywords: Chemical index of alteration (CIA); (HPGe) detector; Radionuclides; geochemistry; Uranophane; Egypt

1. Introduction

In Egypt's Eastern Desert, the southern Sinai Peninsula, and the southwest portion of the Western Desert, one can observe the Precambrian rock formations of the Arabian Nubian Shield. El Sela area is located along the Red Sea coastline in Egypt's southeast desert, between latitudes $22^{\circ}14'28''$ to $22^{\circ}18'3''\text{N}$ and longitudes $36^{\circ}11'51''$ and $36^{\circ}17'20''\text{E}$ (as shown in Fig. 1). It is approximately 27 kilometers the seaside highway west of Abu Ramad City. The terrain in the study area is predominantly moderate to low elevation. Depending on their field relationships and observations the studied rock types in the study area are arranged chronologically, into the following older granite, biotite granite, muscovite granite and two mica granites. The radioactivity of igneous rocks, like granite, is generally higher than that of sedimentary rocks. Nonetheless, some sedimentary rocks, like phosphate and shale rocks, are distinguished from other sedimentary strata by their comparatively high radioisotope concentrations [1,2]. The most common kind of plutonic rock in the continental crust of the Earth is granite. High concentrations of trace elements like uranium (U), thorium (Th) and potassium (K) are found in them; these elements are generally incompatible with the rock's composition. As the magma proceeds through the last stages of differentiation, fractional crystallization, and partial melting, the concentrations of these components increase proportionately to the silica content. Higher amounts of U and Th in granitic rocks are typically occurs in accessory minerals, such as orthite, monazite, apatite, zircon, and titanite. Furthermore, granite contains a wealth of potassium-rich rock forming minerals such mica and feldspar [3,4] mineralization across various global regions. Studying the behavior of radionuclides in geological samples is crucial for gaining insights into how radioactive elements interact with the Earth's geosphere. These radionuclides, which are unstable isotopes that emit radiation during decay, play a key role in understanding natural radioactivity and its environmental impacts.

Granites are extensively acknowledged as some of the most conducive rocks for uranium and predominantly found in anatectic melts in highly peraluminous two-mica granites [5-7]. The main sources of natural radionuclides are environmental radioactivity, primarily due to the presence of ^{238}U , ^{232}Th , and ^{40}K in two-mica granites. Uranium primarily exists in two states of oxidation: U^{4+} and U^{6+} . The U^{6+} state is soluble in the form of the uranyl ion $(\text{UO}_2)^{2+}$, while the U^{4+} state is insoluble in a reducing environment. In contrast, thorium is stable

*Correspondences author: sheriftaalab@azhar.edu.eg (Sherif A. Taalab)

Received date 13 January 2025; Revised date 09 February 2025; Accepted date 15 February 2025

DOI: 10.21608/ejchem.2025.352763.11161

©2025 National Information and Documentation Centre (NIDOC)

and insoluble when it is in the oxidative form Th^{4+} . Consequently, during secondary carbonate production, U and Th are not integrated, resulting in an initial Th/U disequilibrium [8]. Because of their long half-lives and ability to produce a variety of radioactive offspring, radioactive isotopes like uranium (U) and thorium (Th) pose serious dangers to the environment and public health. The chemical weathering of rocks represents a significant process that alters the earth's surface and plays a crucial role in the geochemical distribution of elements. Major oxide and trace element mobilization and redistribution during weathering is a complicated situation because of the impact of several processes, including as ion exchange, co-precipitation, secondary phase development, and primary mineral dissolution [9-11].

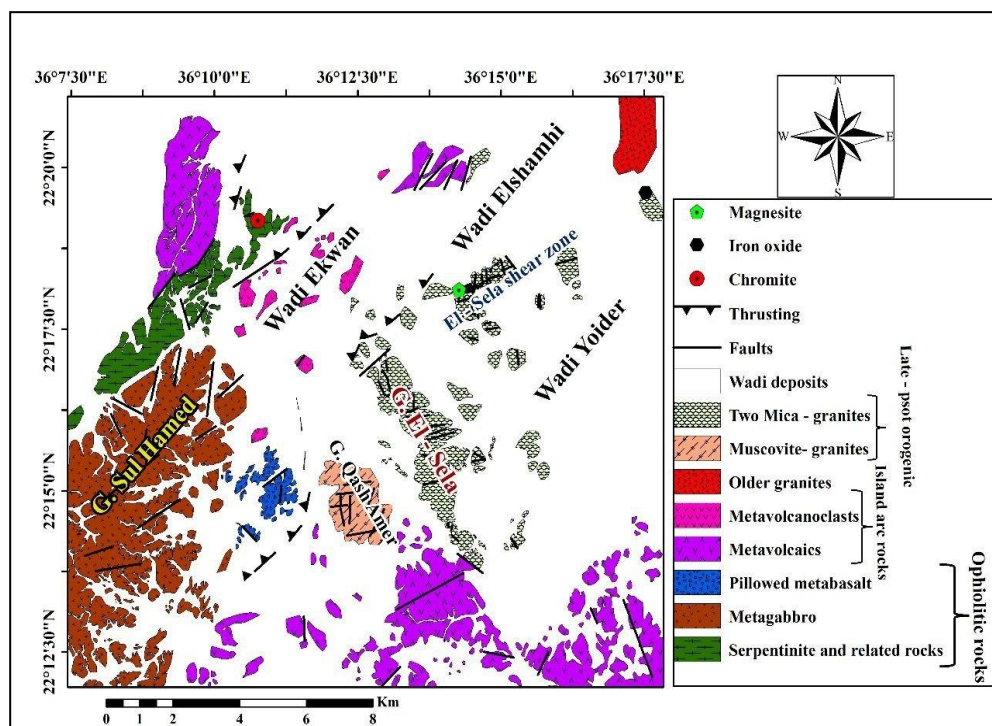


Fig. 1: Geologic map of El Sela area modified after [20].

El Sela granites are considered one of Egypt's most promising regions for uranium mineralization. The El Sela region, part of the Arabo-Nubian Shield, consists of Late Precambrian basement rocks formed during the Pan-African tectono-thermal event. This area in Egypt's Eastern Desert is well-known for its highly weathered, uranium-rich granites [12-15]. Several studies have emphasized that the area's significant potential for uranium deposits [16-18]. According to [19], ^{238}U and some of its offspring were reallocated following the installation of the rock and exposure to various alteration processes. The redistribution of radionuclides in various types of rock is influenced by the acidic and alkaline alteration. With the production of visible U-mineralization, the primary alteration processes are ferrugination, silicification, argillization, and flourization.

In their investigation of the younger granite in the El Sela area, [20] found that, particularly in the Sela shear zone, the younger granite exhibited a high level of incompatible elements like Zr and big ion lithophiles like Sr and a very low content of suitable elements like Cr and Ni. Analyses of major oxides and minor elements showed peraluminous nature and calc alkaline affinity. The ratio of light to heavy REEs is higher than the norm for granite worldwide, whereas the average Σ REE in the granite under study was lower than the average for granite worldwide.

El Sela granite is regarded by [21] as one of the most promising uranium mineralization in Egypt's southern Eastern Desert. The El Sela shear zone, which has ENE-WSW and NNW-SSE trends, is the subject of the current study. It is an ideal bath way for ascending hydrothermal solutions and meteoric water, which caused uranium to leach from its bearing minerals and redeposit in the altered granites. Using a hyper-pure germanium detector, radionuclide activities for ^{238}U , ^{235}U , ^{234}U , ^{230}Th , ^{232}Th , ^{226}Ra , ^{214}Bi , ^{214}Pb , ^{210}Pb , and ^{40}K were detected in the samples under study. Additionally, the following activity ratios were computed: $^{234}\text{U}/^{238}\text{U}$, $^{230}\text{Th}/^{238}\text{U}$, $^{230}\text{Th}/^{234}\text{U}$, $^{226}\text{Ra}/^{238}\text{U}$, $^{226}\text{Ra}/^{230}\text{Th}$, $^{238}\text{U}/^{235}\text{U}$, and $^{234}\text{U}/^{235}\text{U}$. This study's main goal was to examine mineralogy and pinpoint the critical elements affecting radionuclide mobilization in a two-mica granite environment during the course of their history.

2. Experimental (Materials and Methods)

Fieldwork activities involved collecting samples and documenting their spatial relationships. Ten thin sections of the two mica granites were analyzed to ascertain their texture and mineralogy using a polarizing microscope. Following nitric acid digestion and lithium metaborate/tetraborate fusion, 0.2 g samples were subjected to ICP-OES analysis to ascertain major oxide and minor element abundances. Major oxide and trace element concentrations of chosen samples were ascertained using X-ray fluorescence spectrometry at the National Research Center Laboratories, Doki, Egypt. Common oxides such as Al_2O_3 , CaO , Fe_2O_3 , K_2O , Na_2O_3 , MgO , MnO , P_2O_5 , and TiO_2 and trace elements Zn, Rb, Sr, Zr, Ba, Hf, Y and other impurities can be present in various materials and substances. Gamma-ray spectroscopy measurements were conducted on samples in a radiation protection laboratory using a high-purity germanium (HPGe) detector with a relative efficiency of 40% and a full width at half maximum (FWHM) of 1.92 keV for the ^{60}Co gamma energy line at 1332 keV. Gamma radiation was detected and examined using the Canberra Genie 2000 software platform. To reduce background radiation, the HPGe detector was housed in a low-background lead castle that was 4 inches thick. This castle was lined with 1 mm of tin and 1.6 mm of copper to mitigate the effects of lead fluorescent X-rays and bremsstrahlung. The specific activities of ^{238}U and ^{232}Th were inferred indirectly by analyzing gamma ray data. Mineralogical studies were conducted on mineralized and altered samples from the two mica granites. The selected samples were initially crushed using a small hammer to break them into smaller pieces. Subsequently, they were ground to a particle size of 100 to 170 mesh, as determined by microscopic examination, to ensure liberation of individual mineral grains. The samples were processed by washing, drying, sieving, and density separation with bromoform. The heavy fractions were separated into smaller groups based on their magnetic properties using a machine called a Frantz isodynamic separator. This machine sorts of materials by applying different levels of magnetic force (0.2, 0.5, 0.8, 1.0, and 1.5 Amps). Individual mineral grains were carefully selected from each of the separated heavy fractions using a microscope. These selected grains were then examined in further detail at the Nuclear Materials Authority (NMA) using a specialized microscope known as an Environmental Scanning Electron Microscope (ESEM, Phillips XL-30). An electron beam of 25–30 keV, 1–2 mm in diameter, and 60–120 s of counting time was used in the ESEM examination. For 180 seconds, SEM-EDX analyses were carried out for certain locations that were chosen to be around the cores of the mineral grains. Utilizing SEM-EDX, the morphological features of these minerals were also examined. XRD analyses using ZAF correction parameters were carried out at the Egyptian Geological Surveys Central Laboratories in Cairo under 20 kV accelerating potential operating conditions.

3. Geologic Setting

El Sela granites mainly covered by two-mica granites, muscovite granite, and biotite granite. They extruded younger different types of dikes, micro granite, dolerite, bostonite and invaded by pegmatite and quartz veins. El Sela younger granites are pink to red in color and medium to coarse in grain size, they are characterized by cavernous exfoliation, highly weathering (Fig. 2a). Two mica granites are distinguished by the presence of iron and manganese oxides that fill in fractures and joints, demonstrating the iron oxide enrichment of this granite (Fig. 2b) and uranophane in altered two mica granite (Fig. 2c). In the study area, biotite granites are found in the eastern and southern regions as well as display in the western part, they are pink to reddish in color, medium to coarse grained, low to moderate relief. Muscovite granites exposed in the southern part of the study area as medium to coarse grained, massive, pink to red in color. It contains halos around radioactive in minerals (Fig. 2d). The microgranite dike, which ranges in thickness from 3 to 20 meters and is pink to red in color, is strongly enriched with U-mineralization association with iron oxides and crosses the ENE–WSW major shear zone in two-mica granite. U mineralization (uranophane) is adsorbed by microgranite samples stained with iron oxides at the main shear zone of the G. El Sela area (Fig. 2e). Bostonite dike have ENE-WSW and NNW-SSE trends. highly fractured and altered. Its thickness ranges from 1 cm to 2 are fractured, jointed, and vary in thickness from 0.8 to 3 m, mainly composed of microcline, quartz and iron oxide. Their main trends are N-S, NW-SE, and NE-SW (Fig. 2f). White quartz veins dissected two mica granite, ranging in thickness from 1 to 4 m and are positioned near the shear boundaries. Jasprid veins color from reddish gray, run parallel to the older milky quartz vein and two shear zones. Many alteration haloes are present indicating high fluid phases were associated with the different magmatic activities in the area. These modifications Main shear zone (ENE-WSW) is mostly connected to silicification, kaolinization, ferrugination, illitization, and fluoridization.

4. Results and Discussion

4.1. Petrography

Two-mica granite composed of quartz, plagioclases, K-feldspar, biotite and muscovite. Quartz is found as subhedral to euhedral crystals with medium to coarse grain sizes with wavy extinction. K-feldspar are represented by microcline and microcline perthite, as anhedral crystals of patch perthite and string perthite (Fig. 3a). Plagio-

classes occur as subhedral to euhedral crystals. Some crystals are partially altered to epidote and muscovite (surrations zone) (Fig. 3b). Biotite occurs as subhedral flakes, it encloses finer to medium-sized grains of apatite and opaque minerals especially along cleavage planes which might contain radioactive minerals in an amorphous form (Fig. 3c). Zircon, cassiterite and titanite are the main accessory minerals. The opaque mineral linked to plagioclase includes zircon exhibiting color and zonation (Fig. 3d). Biotite granite is composed of quartz, K-feldspar, plagioclase and biotite. Quartz crystals varies in size from medium to coarse grain to subhedral to euhedral, with some exhibiting poikilitic structure. Plagioclase is found as subhedral to euhedral crystals and range in composition from oligoclase to albite. A small amount of iron oxide and quartz are linked to plagioclase anti perthite (Fig. 3e). The orthoclase micro perthite and microcline perthite crystals occur as anhedral to subhedral. Certain microperthite crystals and quartz are linked to plagioclase antiperthite (Fig. 3e). Certain microperthite crystals are euhedral and contain finer albite crystals (Fig. 3f). Microgranite dikes have an equigranular texture and are mainly composed of quartz, K-feldspar, plagioclase, biotite, and muscovite and can range in color from pink to gray (Fig. 3g). Plagioclase varies in grain size between euhedral to subhedral crystals and dolerite dikes are gray to dark gray, with medium- grain size. Plagioclase phenocrystal, pyroxene and hornblende, are usually diabasic textures (Fig. 3h). Pyroxene is predominantly represented by augite and mostly altered to hornblende.



Fig. 2: Photograph showing the different features in younger granite: a) cavernous weathering in two mica granite, b) uraniferous iron oxide filling joints in altered two mica granite, c) trenches in altered two mica granite where uranophane and iron oxide filling fracture and joint in altered microgranite, d) halos around radioactive mineral in muscovite granite, e) microgranite rich in uranophane mineral, f) bostonite dyke extruded two mica granite.

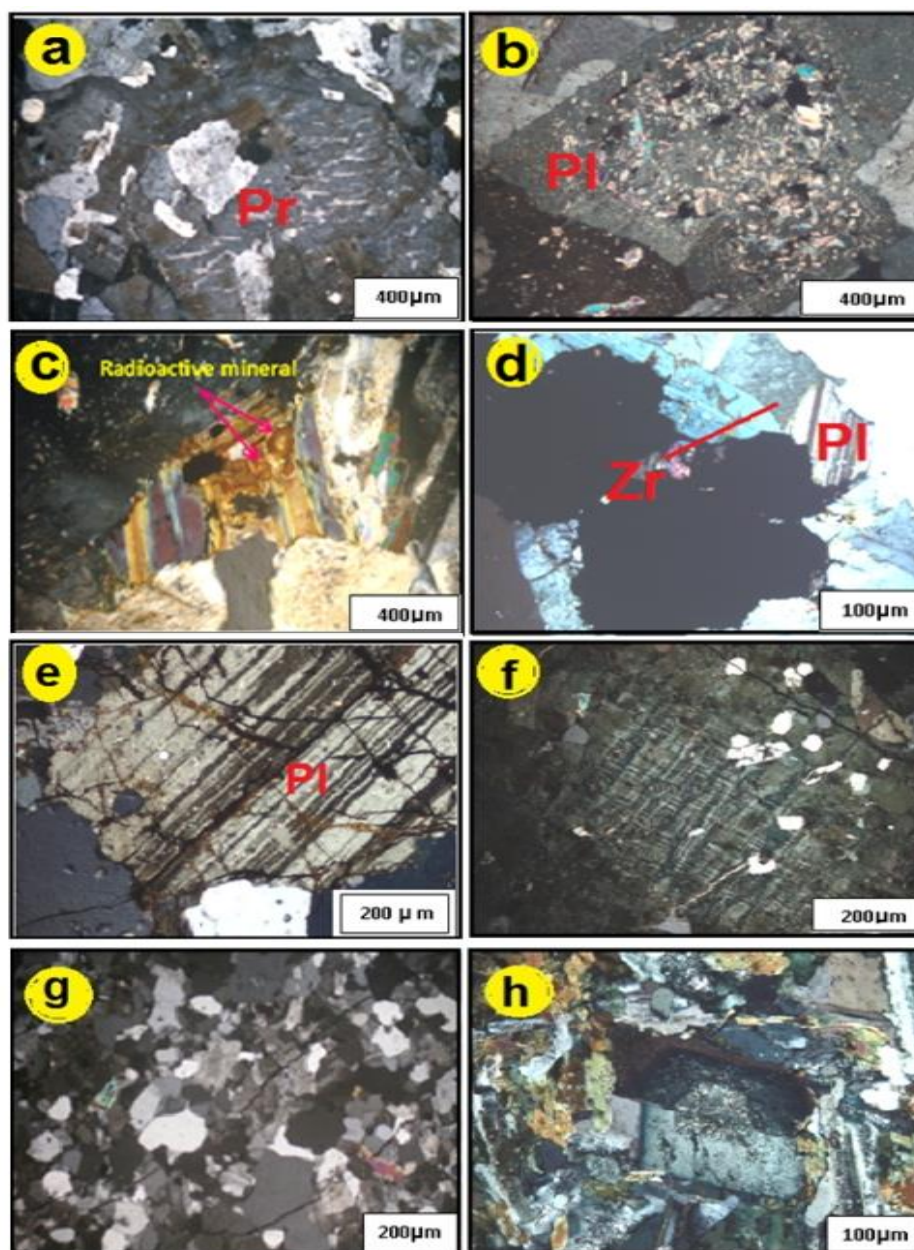


Fig. 3: Photograph showing: a) string perthite encloses quartz crystals perthite, b) Altered muscovite, c) partially altered biotite to chlorite and encloses radioactive mineral, d) zircon crystal enclosed in opaque mineral associated with plagioclase, e) micro crystal of plagioclase filled by iron oxide, f) microcline perthite enclosing fine crystal of albite, g) equigranular texture of microgranite dike, h) dibasic texture in dolerite dike.

4.2. Radionuclide Distribution in the Uraniferous Two Mica Granites

The studied two mica granite samples that were measured radiometrically for determination of radioelement contents ^{238}U , ^{235}U , ^{226}Ra , ^{232}Th and ^{40}K by HPGe-detector. ^{238}U activity concentration range from 324.6 ± 4.7 Bq kg^{-1} to 2401.5 ± 26.2 Bq kg^{-1} with an average 1030.46 ± 10 , ^{235}U from 14.6 ± 1.2 to $88.7 \pm \text{Bq/kg}$ with an average 42.26 ± 2.54 Bq kg^{-1} , ^{232}Th from 68 to 1008.5 Bq kg^{-1} with an average 311.03 Bq kg^{-1} , ^{226}R range from 132.9 ± 6.1 to 184.2 ± 8.2 Bq kg^{-1} with an average 158.55 ± 7.5 Bq kg^{-1} and ^{40}K from 52.7 ± 16.4 to 4531.7 ± 73.2 with 1310.54 ± 23.2 Bq kg^{-1} as an average (Table 1). The uranium, thorium, radium, and potassium activity concentrations in each sample exceeded a worldwide average of 33, 32, 45, and 412 Bq kg^{-1} , respectively [22]. Based on the uranium contents in the two mica granite samples ranging from 26.1 to 193.7 with an average 75.93 ppm, which are more than twice of Clark value [23], these granites will be characterized as uraniumiferous granites [23-29]. Thorium concentration ranges from 3.2 to 121.9 with an average (37.84 ppm), supposing that these granites intimate to high uranium- high thorium granites [30].

4.3. eTh/eU Ratio

Geochemically, uranium and thorium are stable during magmatic crystallization. For this reason, Th/U ratio may be settled over magmatic differentiation [26,28]. In granites, [31] clarified that Th/U ratio (3.5 to 4), may show increments or decrements relative to these values. This could occur according to the prevalent oxidation-reduction conditions, the volatile content, or alterations by endogen or supergene solutions [28,32-35]. The uraniferous granites under study have an eTh/eU ratio of 0.53 (<1), suggesting uranium enrichment in reducing conditions [28,36]. Two micas are suitable as uranium-bearing granites, as shown by their Th/U ratios below (Table 2), which also show the potential for these granites to produce a sufficient uranium source for regional mineralization [37]. An important radiometric technique for determination of U-mineralization is the eU/eTh ratio. The U/eTh ratio was utilized [21,37-40] to characterize the redox conditions; nevertheless, U exhibits an unclear link with which U mobilized (Fig. 4). The U/Th ratio is more than 1 in the productive uriferous rocks [39,41,42]. Uraniferous granites have average U/Th ratios between 0.70 and 10.94, which suggests that the granitic varieties under study are very productive.

Table 1: Radionuclides content in Bq/kg uranium isotopic ratio for the rocks under study.

Parent nuclide	Two mica granite					
	55 S	60 S	31 S	18 S	10 S	13 S
²³⁴ Th	653.8 ±4.7	324.6 ±26.2	2401.5 ±14.9	782±5.2	1364.1 ±7.6	848.8 ±6.1
²³⁴ U	453.1	350.8	1157.4	657.5	1374.1	610
²³⁰ Th	97.5	466.6	430.3	366.9	200.39	328.7
²²⁶ Ra	184.2 ±8.2	132.9±6.1	--	--	--	--
²¹⁴ Pb	83.41.2±1.2	100.5 ± 1.3	343.1 ± 4.4	104.1±14	195.5 ± 1.8	74.1±1.2
²¹⁴ Bi	66.4±15	87.9±1.7	298.3 ± 6.4	95.6 ±1.8	172.2 ± 2.2	64.1 ±1.4
²²⁶ Ra Av.	111.3	116.6	320.7	99.85	183.85	69.1
²¹⁰ Pb	309.4 ± 2.9	297.1 ± 2.4	1172.2 ± 8.7	349 ± 3.1	460 ± 3.7	304 ± 3
²³⁵ U	35.1 ± 1.2	14.6 ± 1.3	88.7 ± 6.5	56.4 ± 2.1	59.1 ± 1.8	39.2 ± 2.2
²²⁸ Ac	147.6 ± 3.2	151.3 ± 3.1	479.4 ± 11.5	178.9 ± 2.9	142.7 ± 2.9	127.9 ± 2.5
²⁰⁸ Tl	141.4 ± 2.8	149.2 ± 2.8	505.2 ± 10.9	183.5 ± 3	153.7 ± 3	129.7 ± 2.6
Av.	1008.5	150.25	492.3	181.2	148.2	128.8
40K	52.7± 17.2	1041.4 ± 17.6	4531.7 ± 73.2	1030.4±16.8	968.6±16.4	1151.4 ±17.1
²³⁸ U PPM	35.0	26.1	193.7	62.8	110.0	68.5
²³² Th PPM	3.2	37.2	121.9	44.9	36.7	31.9
⁴⁰ K %		3.3	14.5	3.3	3.1	3.7
²³⁸ U/ ²³⁵ U	18.28	22.6	27.1	19.81	23.08	21.65
²³⁴ U/ ²³⁵ U	15.39	24.44	19.93	16.8	22.3	15.6
²³⁴ U/ ²³⁸ U	0.69	1.08	0.48	0.84	1.01	0.72
²³⁰ Th/ ²³⁸ U	0.15	0.51	0.18	0.47	0.15	0.39
²³⁰ Th/ ²³⁴ U	0.23	0.48	0.37	0.56	0.15	0.54
²²⁶ Ra/ ²³⁸ U	0.14	0.41	0.15	0.25	0.14	0.07
²²⁶ Ra/ ²³⁰ Th	0.93	0.51	0.18	0.47	0.15	0.39
²¹⁰ Pb/ ²²⁶ Ra	3.43	2.22	3.29	1.76	2.33	4.98
²¹⁰ Pb/ ²³⁸ U	0.47	0.92	0.49	0.45	0.34	0.36

4.4. Geochemical Characteristics

Two mica granites were subjected to chemical analyses for major oxides and trace elements of the sample collected, as indicated in Table 2. The results obtained made it clear that the granitic rocks under study are primarily composed of SiO₂, Al₂O₃, K₂O, and Na₂O as major oxides, with the other oxides having smaller contents. The average SiO₂ concentration is 68.22 wt.%, with the greatest value reaching 71.55 wt.% and the lowest being 54.44 wt.%. The range of FeO^t, CaO, Al₂O₃, Na₂O and K₂O is 0.59-13.51, 0.60-0.88, 15.19-21.13, 0.26-3.83 and 5.04-7.63 wt.% respectively. The concentration of trace elements differed considerably from the rocks under study. Zinc (Zn) contents were low in two mica granite and range from 12.4-17.1 ppm; rubidium (Rb) reaches up to their highest contents 244 ppm. Strontium (Sr) contents range from 32 to 109 ppm. All samples in (Table 2) have very low concentration from nickel (Ni) which ranges from 2.5 to 5.1 ppm, zirconium (Z) reaches up to 95 ppm. Hafnium (Hf) and tantalum contents were low and range from 2.98 to 5.3 and 9.20 to 15.4 ppm whereas barium (Ba) values were high in two mica granite and reaches up to 278.1. The relation between U and some trace elements exhibits a weak positive correlation with Rb and moderate positive relation with Hf. On the other hand, U shows ill-defined correlation with Nb, Ta, Y and Sn (Fig. 5). Rb increases with increasing K-feldspar and sericite. According to [43], Rb content increases in liquids that are concentrated during late magmatic differentiation and include a lot of volatile components. In granites, the chondritic ratio is 38 [44], and the average

Zr/Hf value is 39 [45]. Zr/Hf ratio decreases with increasing evolution of the silicate melt. The Zr/Hf value in the granites under study is 17.5, suggesting highly evolved granite [46], and clarify the redistribution and uranium migration with other elements during late stages processes.

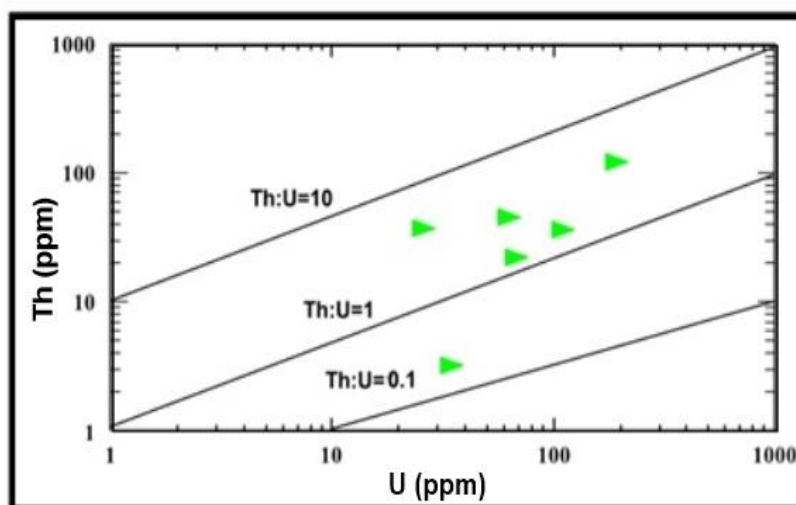


Fig. 4: Diagram of Th-U variation for the sample under study.

4.5. Chemical Index of Alteration

Features that influence chemical composition, including the extent of source weathering, must be briefly considered. The chemical index of alteration $\{CIA = [Al_2O_3 / (Al_2O_3 + CaO + Na_2O + K_2O)] \times 100\}$ has been interpreted as a measure of significant oxide changes brought on by weathering and the transformation of volcanic glass, feldspars, and other labile elements into clay minerals. Therefore, the CIA may be a helpful index for classifying various rock types according to their varying source terrains. The average CIA values for shale around the world are between 70 and 75; values for new granites are about 50 [47], and extensive weathering may result in values close to 100 [48]. Two mica granite samples have CIA values between 56.80 and 77.68 with an average 60.79, which are indicative of moderately to strongly weathered source terrain. It is evidenced that increments in the chemical index of Alteration samples show fractionation of uranium and of alteration (CIA), is accompanied by decrements in both uranium and thorium, exhibiting uranium leaching during alteration processes and adsorption of thorium on clay minerals resulting from granite alterations (Fig. 6a-d). Also, $^{234}U/^{238}U$ and $^{230}Th/^{234}U$ are constant during alteration process due to ^{234}U leaching by circulating solutions.

4.6. Activity Ratios (AR's)

The radionuclides ^{238}U , ^{234}U , and ^{230}Th achieve radioactive equilibrium in closed geologic systems after 1.7 Ma [49], with activity ratios of $^{230}Th/^{234}U$, $^{230}Th/^{238}U$, and $^{234}U/^{238}U$ all equalling unity. If the systems are exposed to weathering changes, or groundwater movement, the different physicochemical circumstances affecting ^{238}U and ^{234}U will cause their fractionation, and as a result, the corresponding daughter/parent radionuclide activity ratios in the decay series will diverge from unity. U isotopes fractionation is mainly related to the selective leaching of ^{234}U by the direct α -recoil transfer of a ^{234}U precursor (^{234}Th). When the $^{234}U/^{238}U$ activity ratio is less than or larger than 1, it means that a uranium isotope has moved within the rock within the last 1–2 million years, which is how long it takes for ^{234}U to attain secular equilibrium [50,51,21,27]. The activity ratios of various radionuclides in the altered two mica granites are registered in Table (1). The activity ratios of $^{238}U/^{235}U$ for each sample under study ranges from 18.28 and 27.1 with an average of 22.09 which indicate the shifting of this ratio positively and/or negatively from the natural ratio (21.7), exhibiting the role of the alteration processes in redistribution of ^{238}U and ^{235}U in various samples as shown in Fig. (7). The altered granite samples $^{234}U/^{235}U$ ratios range from 15.39 to 24.44, with an average of 19.08. This indicates that most samples have uranium-234 leaching out as a result of alteration activities. ^{234}U is more mobile than other uranium isotopes because it is produced from ^{238}U by α -decay and then deposited at crystal sites that have been damaged by α -recoil. Due to uranium-containing materials weathering in water, ^{234}U preferentially leaches from these α -damaged crystal sites [52]. The $^{234}U/^{238}U$ average activity ratio is 0.80, with a range of 0.48 to 1.08, manifesting ^{234}U migration out in the studied rocks through the prevailing oxidation-reduction conditions in the alteration processes. $^{234}U/^{238}U \leq 1$ and $^{230}Th/^{234}U > 1$ are typical traits of uranium extraction from rocks [53]. Whilst $^{234}U/^{238}U < 1$ and $^{230}Th/^{234}U < 1$ in the two mica

granites, which could be resulted from the late adsorption of thorium by organic matter, clay minerals and or/iron oxides in the altering solutions. While U is immobile in a reducing environment and only becomes soluble in oxidizing settings, radium is rapidly mobilized in reducing conditions and readily adsorbed onto minerals generated in oxidized zones, such as iron hydroxides.

The $^{226}\text{Ra}/^{238}\text{U}$ activity ratio is also an excellent signal for alteration processes and migration of either ^{238}U or ^{226}Ra depending on the pH that prevailed, according to [54]. The activity ratios of $^{226}\text{Ra}/^{238}\text{U}$ indicate that there is disequilibrium between ^{238}U and ^{226}Ra and reflect lesser than 1 for most studied sample except for one sample (60S) as shown in Fig. (8), accumulation of ^{238}U or migration out of ^{226}Ra resulting from recoil-implanted ^{226}Ra atoms from decay of ^{230}Th atoms and Ra readily adsorbed on to clay mineral in the solution. $^{226}\text{Ra}/^{238}\text{U}$ ratio in all the studied granites (<1) may be related to the unusual high amounts of ^{238}U .

Table 2: Chemical composition of El Sela two mica granite

S. No.	10S	18 S	31S	13S	60S	55 S
Major oxides (Wt%)						
SiO ₂	71.11	70.88	70.26	71.55	54.44	71.12
TiO ₂	0.08	0.17	0.17	0.19	1.9	0.13
Al ₂ O ₃	15.80	15.58	16.07	15.29	21.13	15.44
FeO ^t	0.59	1.16	0.98	1.32	13.51	1.09
MnO	0.04	0.05	0.09	0.02	0.03	0.03
MgO	0.13	0.17	0.15	0.16	0.91	0.13
CaO	0.68	0.88	0.77	0.64	0.77	0.60
Na ₂ O	3.83	3.73	3.37	3.36	0.26	3.58
K ₂ O	7.03	7.04	7.63	7.09	5.04	7.56
P ₂ O ₅	0.05	0.03	0.05	0.03	0.63	0.02
L.O.I	0.46	0.28	0.44	0.30	1.10	0.22
Total	99.8	99.7	99.98	99.95	99.77	99.92
CIA	57.79	57.21	57.28	58	77.68	56.80
Trace elements (ppm)						
Zn	17.1	14.3	14.3	15.3	19.5	12.4
Rb	233	137	244	188	214	195
Sr	33	45	47	32	109	51
S	0.040	0.039	0.040	.039	0.45	0.040
Zr	40	39	77	95	90	40
Pb	21	20	19.2	23.7	30.7	22.4
Ba	278.1	222	200	245.3	191	121.5
Ni	3.4	3.3	2.5.	3.2	5.1	2.4
Hf	4.37	3.65	5.3	3	2.98	4.57
Y	8.2	5.3	7.1	16	18.10	7.12
Ta	15.4	11.7	10.50	9.20	14.4	13.11
Nb	7.2	5.4	3.4	12	17.10	5.99
U	4.6	5	6.40	5.23	7.80	4.40
Th	20.12	20.1	23.4	20.45	28.89	20.13
Zr/Hf	9.15	10.68	14.53	31.67	30.20	8.75

$^{226}\text{Ra}/^{230}\text{Th}$ ARs of the examined samples are also less than unity which could be connected to the adsorption of ^{230}Th on clay minerals and iron oxides that are the outcome of alteration processes (Fig. 7). It is common to find the short-lived lead nuclide ^{210}Pb in secular equilibrium with ^{226}Ra . There are few exceptions to this rule, such as aqueous systems where ^{210}Pb is preferentially removed due to its insoluble character or conditions where ^{222}Rn is lost from the system by degassing [55]. $^{210}\text{Pb}/^{226}\text{Ra}$ ARs are higher than one for all of the samples indicating radon accumulation leading to ^{210}Pb enrichment. The reverse case is registered on $^{210}\text{Pb}/^{238}\text{U}$ ratio which is less than unity due to ^{238}U enrichment. Thiel's diagram is interpreted as the U-series disequilibria (Fig. 9) and controlled by the relation between $^{230}\text{Th}/^{238}\text{U}$ and $^{230}\text{Th}/^{238}\text{U}$ [56]. The diagram is classified into different segments determined by (i) the $^{234}\text{U}/^{238}\text{U}$ equilibrium line (AR = 1) and (ii) the line that results from drawing a tangent on the closed system chain decay curves evolving towards radioactive equilibrium ($^{230}\text{Th}/^{238}\text{U} = 1$ and $^{234}\text{U}/^{238}\text{U} = 1$) following the sudden buildup and destruction of uranium. Segments I and II between the zones where uranium is added or removal indicate imbalances in the uranium series, which cannot be produced through the decay process in a closed system.

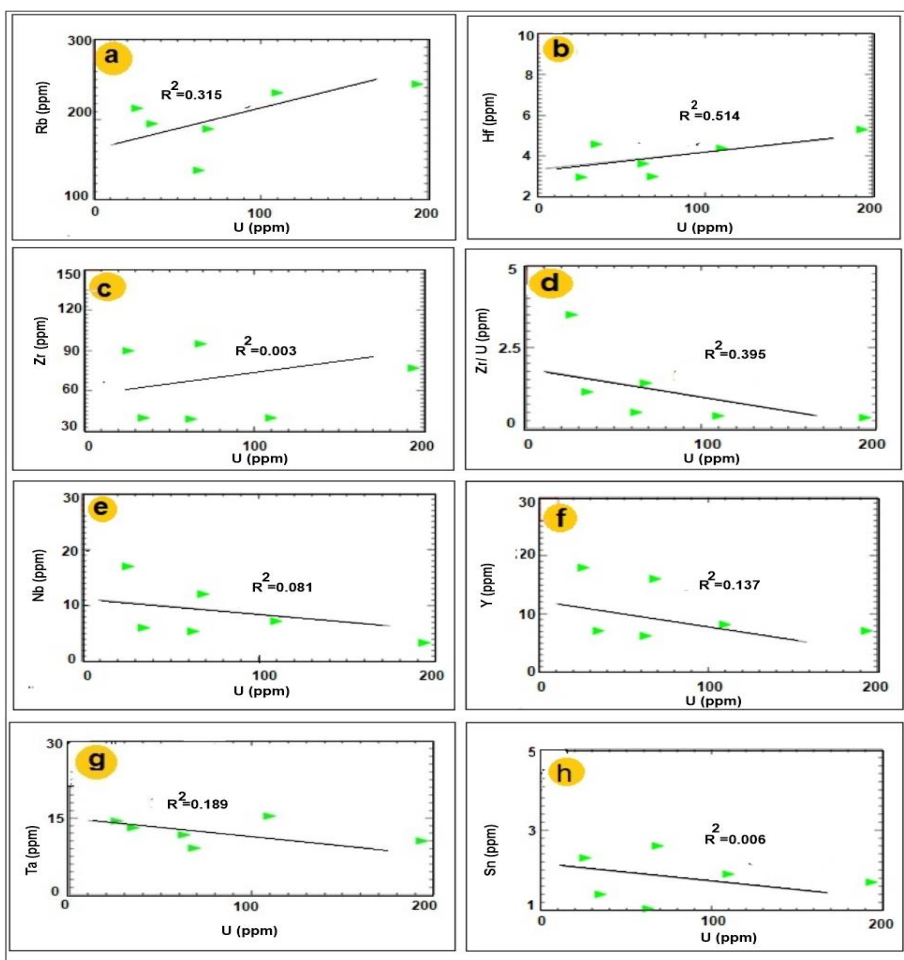


Fig. 5: U variation diagram vs Rb (a), Hf (b), Zr (c), (d) Zr/u, Nb (e), Y (f), Ta (g) and Sn (h)

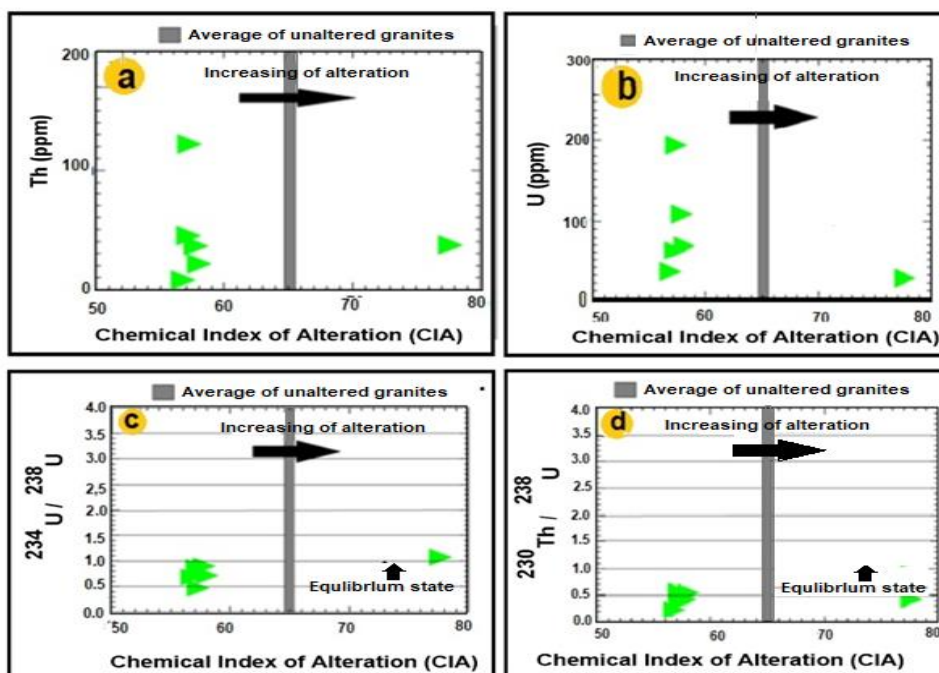


Fig. 6: Binary diagram between (CIA) versus a) $^{234}\text{U}/^{238}\text{U}$, b) $^{230}\text{Th}/^{234}\text{U}$ c) Th (ppm), d) U (ppm) for the studied two mica.

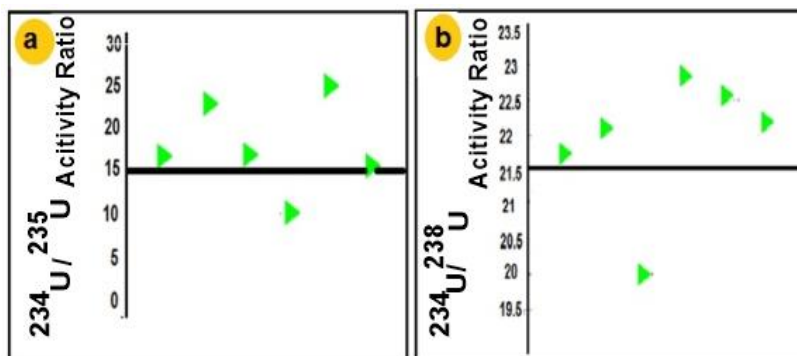


Fig.7: a) Variation of the $^{234}\text{U}/^{235}\text{U}$ activity ratio for studied samples. b) Variation of the $^{238}\text{U}/^{235}\text{U}$ activity ratio studied samples.

In segment I, the plots indicate an open system that prefers the removal of ^{234}U . An open system influencing bulk uranium is represented by the uranium series disequilibria identified by segment II. These data include uranium removal samples and samples of newly accumulated uranium (during the last million years) [57]. The plot of $^{234}\text{U}/^{238}\text{U}$ against $^{230}\text{Th}/^{238}\text{U}$ (Fig. 9) illustrates the routes to equilibrium for solid phases are displayed for two cases: uranium accumulation (indicated by a decrease in $^{230}\text{Th}/^{238}\text{U}$) and uranium leaching (indicated by an increase in $^{230}\text{Th}/^{238}\text{U}$). All instances of uranium leaching are characterized by a ($^{234}\text{U}/^{238}\text{U}$) activity ratio (AR) less than 1, whereas uranium accumulation cases are defined by a ($^{234}\text{U}/^{238}\text{U}$) AR greater than 1 [42,55]. In the Thiel diagram (Fig. 9), plots of the samples that deviate from secular equilibrium, with values greater than 1.10 or less than 0.90 for $^{234}\text{U}/^{238}\text{U}$, $^{230}\text{Th}/^{238}\text{U}$, $^{230}\text{Th}/^{234}\text{U}$, and $^{226}\text{Ra}/^{230}\text{Th}$, fall into the forbidden region. This is a complex geochemical zone where the systems can be identified as having undergone complex U migration. Most of the two mica samples lie in the forbidden sector zone (disturbed conditions continue removal and leaching) with exception of two samples, one at the equilibrium line and the other in the accumulation zone. The plot of the $^{238}\text{U}/^{234}\text{U}$ activity ratios against $^{230}\text{Th}/^{234}\text{U}$ activity ratios (Fig. 10) show that the two mica granite samples have been affected by leaching-accumulation events in the period from ($>3 \times 10^4$ to $>6 \times 10^4$ years).

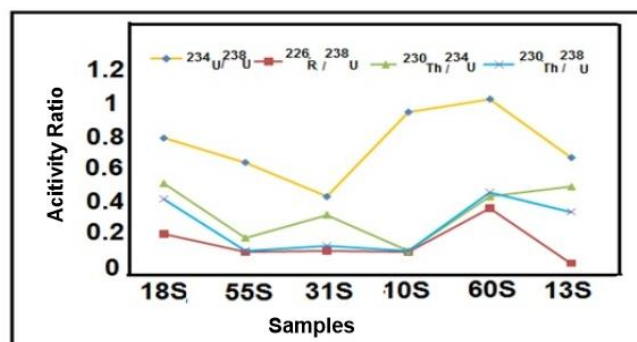


Fig. 8: Variation of the $^{230}\text{Th}/^{238}\text{U}$, $^{230}\text{Th}/^{234}\text{U}$, $^{226}\text{Ra}/^{238}\text{U}$ and $^{234}\text{U}/^{238}\text{U}$ activity ratio in the studied samples

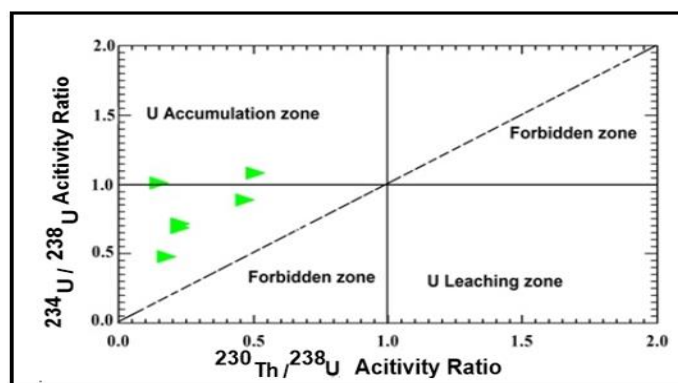


Fig. 9: Thiel diagram showing the evolution of ^{234}U - ^{238}U versus $^{230}\text{Th}/^{238}\text{U}$ activity ratios.

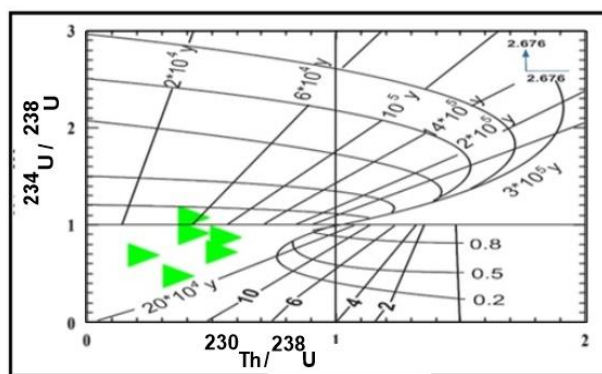


Fig. 10. $^{234}\text{U}/^{238}\text{U}$ and $^{230}\text{Th}/^{238}\text{U}$ activity ratios for the samples studied. The curved lines show the time-varying trajectories of samples with different initial alpha activity ratios, whereas the straight lines indicate varying ages (after [56]). Activity ratios that are conservatively regarded as being close to or at secular equilibrium are included in the boxed-in area.

4.7. Mineralogical Investigations

The main radioactive and other heavy minerals in the uriferous two mica granites are uranophane, kasolite, autunite, zircon, apatite, titanite, pyrite and rutile. The most prevalent group of uranium minerals are uranyl silicates. Based on their uranium to silicate ratio, these minerals can be classified into a number of groups [58-60]. This group comprises uranophane, beta-uranophane, kasolite, sklodowskite, boltwoodite, sodium boltwoodite and cuprosklodowskite.

Uranophane secondary uranium minerals in nature are characterized by their bright colors (lemon, yellow and brown of many shades). They can be found as fillers for fissures and fractures. In the two-mica granite, uranophane is generally massive with granular forms, subhedral to anhedral, of dull or greasy luster and the color ranges from straw yellow to canary yellow. The hardness of the examined uranophane grains varies from very soft to hard. It is concentrated in the non-magnetic fraction (1.5 amp). EDAX analyses reflect the uranophane composition. Pure sample of uranophane was prepared by hand picking from the fraction of bromoform (sp. gr. 2.85 gm/cm³) and subjected to XRD (Fig. 11 a & b). Kasolite is identified by its bright colors ranging from canary lemon, yellow to various shades of yellow and brown. In contrast to other uranium secondary minerals, kasolite grains are comparatively tougher [61,62]. In general, kasolite crystal habit and brilliance set it apart from the other uranium silicates. The only uranyl silicate with lead as the primary cation is this one, which is a hydrated silicate of lead and hexavalent uranium. Analysis of the kasolite using EDAX indicate that they are consists mainly of lead, uranium and silicon, in addition to impurities of Al, Fe and K. The presence of uranophane was also confirmed by X-ray diffraction (XRD), (Figs. 11 c & d).

Autunite is a secondary uranium mineral that is typically formed altering pitchblende or uraninite and is found in the oxidation and weathering zone. In addition to the soft aggregates of autunite and meta-autunite are lemon yellow to greenish yellow in color. EDAX analyses indicate the autunite composition were confirmed by XRD (Figs. 11 e & f). In most cases, zircon typically appears as short and long euhedral prismatic and/or bipyramidal crystals, in a range of colors including colorless, pale yellow, reddish brown, and reddish orange. The well-formed euhedral shape of zircon indicates its magmatic origin. They are almost colorless, but sometimes dark metaleptic type. In the thin section, it is included in quartz and micas and rimmed by iron oxides. The zircon composition was clarified by EDAX analyses (Fig. 12a). In Earth's surface rocks, pyrite is the most common and abundant sulfide mineral, often being typically makes up the main opaque phase in ore deposits. In contact metamorphic ore deposits and hydrothermal deposits with temperatures ranging from mild to high, pyrite forms large bodies. In the study area, the EDAX analysis indicates that cubic pyrite composed of S (52.7%) and Fe (47.3%) (Fig. 12b). Apatite crystals typically appears as yellowish white colors. Apatite grains rounded and pitted surface indicate that they have undergone transportation. The resulting EDX and BSE images are shown in (Fig. 12c). Titanite in general, it is found as an accessory mineral in igneous rocks. It is a sphenoid-shaped calcium titanium silicate mineral (CaTiSiO₅). Sphene is of rhombic shape and brown in color. It is found in the non-magnetic fraction at the stage of 1.5 amp. The obtained SEM analysis of the investigated titanite (Fig. 12d). Rutile grains exhibit a wide range of color depending on their chemical constitution. This color variation results from impurity ions, particularly ferric iron, niobium, and tantalum, occupying the interior crystal structure. The well-developed euhedral crystals of rutile are usually represented by bipyramidal tetragonal prisms. The primary element compositions of selected rutile grains are significantly enriched in Ti (48.9 wt.%), O (45.8 wt.%) (Fig. 12e), in addition to Mg, Al and Si as impurities.

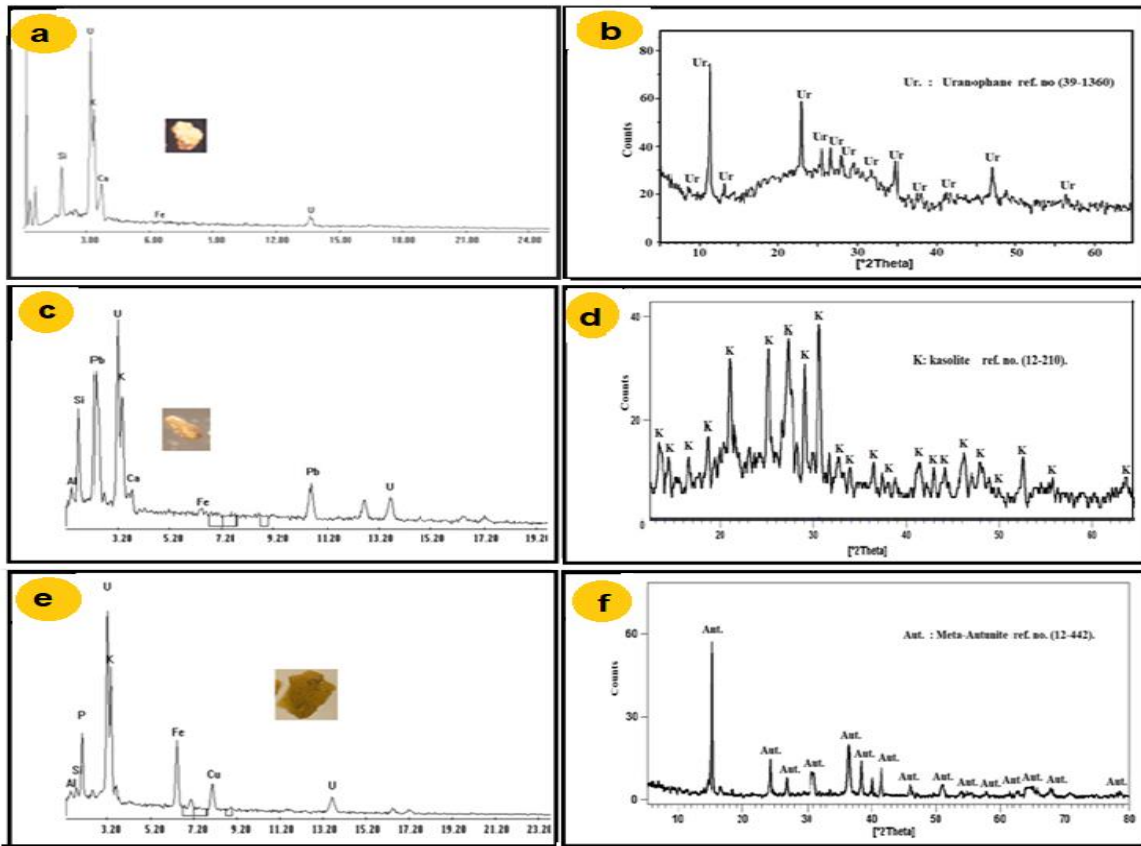


Fig. 11: (a, b) EDX analysis and back-scattered electron imaging (BSE) images for uranophane mineral; and XRD pattern of uranophane minerals (c&d) kasolite mineral and (e&f) autunite mineral

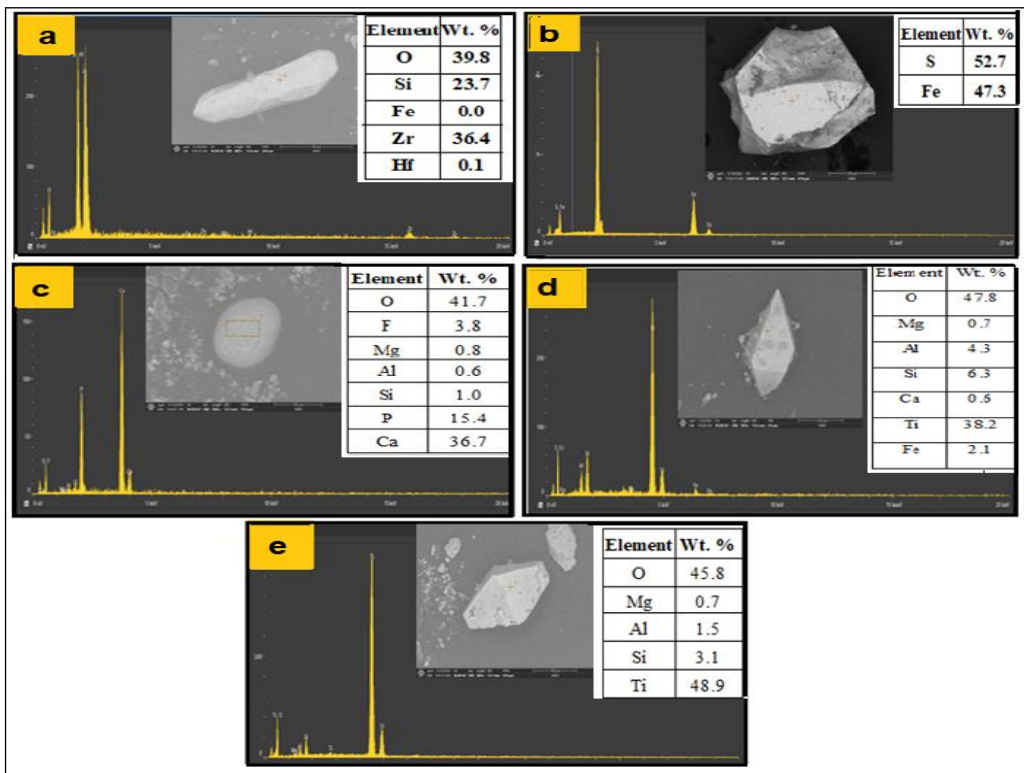


Fig. 12: EDX analysis and back-scattered electron imaging (BSE) images for a) zircon mineral. b) pyrite mineral. c) apatite mineral. d) titanite mineral. e) rutile mineral.

5. Conclusion

El Sela granites are extruded and invaded by younger types of dikes and veins, as microgranite, dolerite, bostonite in addition to pegmatite and quartz veins. Petrographically, the primary hydrothermal alteration processes affecting these granites include sericitization, hematitization, chloritization, kaolinitization, episyenitization and illitization whereas the primary accessory minerals are zircon, cassiterite, and titanite. These granites are of uranium nature. Increments in the chemical index were accompanied by decrements in both uranium and thorium, exhibiting uranium leaching during alteration processes with thorium adsorption on clay minerals. Cross plot between U and some trace elements with Zr/U ratio exhibits the redistribution and uranium migration with other elements during late stages processes. The activity ratios of $^{234}\text{U}/^{235}\text{U}$ and $^{238}\text{U}/^{235}\text{U}$ indicate the shifting of this ratio positively and/or negatively from the natural ratio, exhibiting the role of the alteration processes in the redistribution of ^{234}U , ^{238}U and ^{235}U in various samples. The $^{234}\text{U}/^{238}\text{U}$ activity ratio mostly is lesser than unity, manifesting ^{234}U migration out in the studied rocks through the prevailing oxidation-reduction conditions in the alteration processes. $^{210}\text{Pb}/^{226}\text{Ra}$ ARs are greater than unity for all samples indicating radon accumulation leading to ^{210}P enrichment. The $^{234}\text{U}/^{238}\text{U}$ versus $^{230}\text{Th}/^{238}\text{U}$ activity ratios clarify that most of the two mica samples lie in the forbidden sector zone (disturbed conditions continue accumulation and leaching) with exception of two samples, one at the equilibrium line and the other in the accumulation zone show that the two mica granite samples have been affected by leaching-accumulation events in the period between ($>3 \times 10^4$ to $>6 \times 10^4$ years). Mineralogical investigation studies elucidate that the main radioactive and other heavy minerals in the uraniumiferous two mica granites are uranophane, kasolite, autunite, zircon, apatite, titanite, pyrite and rutile.

6. Conflicts of Interest

“There are no conflicts to declare”.

7. References

- [1]. Tzortzis, M. H., Tsertos, S., & Christofides, G. (2003). Christodoulides, Gamma-ray measurements of naturally occurring radioactive samples from Cyprus characteristic geological rocks, *Radiat. Meas.* 37, 221–229. [https://doi.org/10.1016/S1350-4487\(03\)00028-3](https://doi.org/10.1016/S1350-4487(03)00028-3).
- [2]. Omar, A.E., Sakr, M.A.H., Taalab, S.A., Bakhit, A.B.A., Pugliese, M., La Verde, G., & Hanfi, M.Y. (2023). Geotechnical and environmental radioactivity investigations at Al Sadis Min Uktober city, Cairo municipality (Egypt), for the high-speed railway construction. *Appl. Radiat. Isot.* 193: 110664. <https://doi.org/10.1016/j.apradiso.2023.110664>
- [3]. Orgün, Y., Altınsoy, N.A.H., Gültekin, G., & Karahan, N. (2005). Natural radioactivity levels in granitic plutons and groundwaters in Southeast part of Eskisehir, Turkey, *Appl. Radiat. Isot.* 63, 267–275. <https://doi.org/10.1016/j.apradiso.2005.03.008>.
- [4]. Taalab, A.S., Ismail, A.M., El Maadawy, W.M., Abdelrahman, K., Khandaker, M.U., Sakr, A.K., & Hanfi, M.Y. (2024a). Natural radioactivity, mineralogy and hazard assessment of syenogranites (ornamental stones) using a statistical approach. *Nuclear Engineering and Technology*, 56, 4141–4148. <https://doi.org/10.1016/j.net.2024.05.017>.
- [5]. [5] Ibrahim, M.E., Zalata, A.A., Assaf, H.S., Ibrahim, I.H., Rashed, M.A. (•••). El Sella shear zone, South Eastern Desert, Egypt. Example of vein-type uranium deposit. In: The 9th international mining ,petroleum and metallurgical engineering conference, pp 41–55.
- [6]. Poty, B., Cuney, M., & Friedrich, M. (1986). Uranium deposits spatially related to granites in the French part of the Hercynian Orogeny, vein type uranium deposits. IAEA-TECDOC-361, IAEA, Vienna. 215–246.
- [7]. Ali, K.G. (2013). Structural control of El Sela granites and associated uranium deposits, south Eastern Desert Egypt. *Arab. J. Geosci.* 6, 1753–1767. <https://doi.org/10.1007/s12517-011-0489-y>
- [8]. Scholz, D., & Hoffmann, D. (2008). $^{230}\text{Th}/\text{U}$ -dating of fossil corals and speleothems. *Eiszeitalter Ggw. Quat. Sci. J.* 57(1-2), 52–76. <https://doi.org/10.3285/eg.57.1-2.3>.
- [9]. Abdel Gawad, A., & Ibrahim, E.M. (2016). Activity ratios as a tool for studying uranium mobility at El Sella shear zone, southeastern Desert, Egypt *J. Radioanal. Nucl. Chem.* 308, 129. <https://doi.org/10.1007/s10967-015-4374-0>.
- [10]. Lee, S.Y., Kim, S.J., & Baik, M.H. (2008). Chemical weathering of granite under acid rainfall environment, Korea. *Environ. Geol.* 55, 853–862. <https://doi.org/10.1007/s00254-007-1037-7>.
- [11]. Taalab, S.A., Al Meshari, M., Alzamil, Y., Abanomy, A., Alyahyawi, A.R., Mohamed, W.H., & El-Taher, A. (2023). Radiological and ecological hazards evaluation of episyenite used as building materials. *J. Radioanal. Nucl. Chem.* 332, 2057–2075. <https://doi.org/10.1007/s10967-023-08890-9>.
- [12]. Abdel Gawad, A.E., & Ibrahim, E.M. (2016). Activity ratios as a tool for studying uranium mobility at El Sella shear zone, southeastern Desert, Egypt. *J. Radioanal. Nucl. Chem.* 308, 129–142 <https://doi.org/10.1007/s10967-015-4374-0>

- [13]. Ibrahim, T.M.M., Cuney, M., Ali, K.G., Abdel Meguid, A.A., Gaffar, I.M., Shahin, H., Omar, S.A., Masoud, S.M., & Haridy, H.M.M. (2005). The U fertility Criteria Applied to El Sela Granite, Southeastern Desert, Egypt. International Symp. Uranium Production and Raw Materials for the Nuclear Fuel Cycle, IAEA, Vienna, Austria, 20–24 June 2005, pp. 1103.
- [14]. Gaafar, M.I., Ghazala, H.H., Ibrahim, T.M., & Ammar, S.E. (2006). Gamma ray spectrometry studies for a promising vein type uranium mineralization, Southeastern Desert, Egypt. In: Proc. 4th Internat. Symp. Geophysics, Tanta, Egypt, pp. 445–456.
- [15]. El-Afandy, A.H., Ibrahim, T.M., Ali, K.G., Gaafar, I.M., Masoud, S.M., Omer, S.A., Shahin, H.A., Farag, S.S., Abu Donia, A.M., Aly, E.M., Omran, A.A., Abdel Gawad, A.E., Bayoumi, M.B., El Werdani, M.H., Abdalla, O.K., Abdel Fataah, M.F., Esmat, R.A., Zaher, F.Y., & Hamed, A.A. (2008). Uranium Resources Development, El Sela Site Development Project, Internal Report, Nuclear Materials Authority.
- [16]. Ali, M.A., & Lentz, D.R. (2011). Mineralogy, geochemistry and age dating of shear zone-hosted Nb–Ta-, Zr–Hf-, Th-, U-bearing granitic rocks in the Ghadir and El-Sella areas, Southeastern Desert, Egypt. *Chin. J. Geochem.* 30(4), 453–478. <https://doi.org/10.1007/s11631-011-0531-5>.
- [17]. Ali, K.G. (2011). Structural control of El Sela granites and associated uranium deposits, Southern Eastern Desert, Egypt. *Arab. J. Geosci.* <http://dx.doi.org/10.1007/s12517-011-0489-y>.
- [18]. Khattab, M.R., Mohamed, W.H., Shetaia, S.A., Ahmed, M.S., Taalab, S.A., Saadawi, D.A., Sakr, A.K., Khandaker, M.U., Elshoukrofy, A.S.M., & Hanfi, M.Y. (2024). Radiological, environmental, and structural investigations of Wadi El Markh granitic rocks, southeastern desert, Egypt. *Nuclear Engineering and Technology.* <https://doi.org/10.1016/j.net.2024.06.015>
- [19]. Abdel Gawad, A.E., Orabi, A.H. & Bayoumi, M.B. (2014). Uranium Evaluation and Its Recovery from Microgranite Dike at G. El Sela area, Southeastern Desert, Egypt. *Arab. J. Geosci.* 8, 4565–4580. <http://dx.doi.org/10.1007/s12517-014-1499-3>.
- [20]. El Mezayen, A.M., Heikal, M.A., El-Feky, M.G., Shahin, H.A., Abu Zeid, I.K., & Lasheen, S.R. (2019). Petrology, geochemistry, radioactivity, and M-W type rare earth element tetrads of El Sela altered granites Southeastern Desert, Egypt. *Acta Geochim* 38(1), 95–119. <https://doi.org/10.1007/s11631-018-0274-7>.
- [21]. El Mezayen, A.M., Ibrahim, E.M., El-Feky, M.G., Omar, S.M., El-Shabasy, A.M., & Taalab, S.A. (2022). Physico-chemical conditions controlling the radionuclides mobilization in various granitic environments. *Int. J. Environ. Anal. Chem.* 102, 4, 970–986. <https://doi.org/10.1080/03067319.2020.1729758>
- [22]. UNSCEAR, Sources and Effects of Ionizing Radiation - Exposures of the Public and Workers from Various Sources of Radiation - UNSCEAR 2008 Report, 2010. New York, http://www.unscear.org/docs/reports/2008/09-86753_Report_2008_Annex_B.pdf.
- [23]. Clark, S. P. J., Peterman, Z. E., & Heier, K. S. (1966). Abundances in uranium, thorium and potassium. In: Handbook of physical constants. Geol. Soc. of Amer. Memoir. 97: 521-541.
- [24]. Darnely, A. G. (1982). Hot granite; Some general remarks. In: Uranium in granites (ed), Y.T. Maurice. Geol. Surv. of Canada. 81-23: 1-10.
- [25]. Assaf, H.S., Mahdy, M.A., & El-Afandy, A.H. (1997). Egyptian Younger Granites: an approach to define parameters favoring formation of uranium deposits. 3rd Int. Conf. Geochem., Alex. Univ. Egypt. P.409-420.
- [26]. Raslan, M.F., Ali, M.A., & El feky, M.G. (2010b). Mineralogy and radioactivity of pegmatites from South Wadi Khuda area, Eastern Desert, Egypt. *Chin. J. of Geoch.* 29, 343-354. <https://doi.org/10.1007/s11631-010-0466-2>.
- [27]. El Mezayen, A.M., Abu Zeid, E.K., Hosny, W.S., El-Feky, M.G., Omar, S.M., & Taalab, S.A. (2019). Geochemistry, mineralogy, and radioactivity of the Abu Furad Area, Central Eastern Desert, Egypt. *Acta Geochim* 38, 307–326. <https://doi.org/10.1007/s11631-018-0302-7>
- [28]. El-Fekya, M. G., Mohammed, H. S., El-Shabasy, A. M., Ahmed, M. R., Abdel-Monem, Y. K., & Mira, H. I. (2021). Mobilisation of radionuclides during uranium and gold processing of granitic rock at El-Missikate area, central Eastern Desert, Egypt. *International Journal of Environmental Analytical Chemistry*, 103(16), 4285–4298. <https://doi.org/10.1080/03067319.2021.1925262>.
- [29]. Seif, R.A., Ene, A., Zakaly, H.M.H., Sallam, A.M., Taalab, S.A., Fnais, M.S., Saadawi, D.A., Amer, S.A., & Awad, H.A. (2024). Distribution of Heavy Metals along the Mediterranean Shoreline from Baltim to El-Burullus (Egypt): Consequences for Possible Contamination. *Minerals*, 14, 931. <https://doi.org/10.3390/min14090931>.
- [30]. Taalab, S.A., Zakaly, H.M.H., Ivanov, V., Alrowaily, A.W., Awad, H.A., Abed, N.S., Issa, S.A.M., Eltohamy, A.M., & Ene, A. (2023b). Notable changes in geochemical and mineralogical characteristics of different phases of episyenitization: insights on the radioactive and shielding of the late phase. *Front. Earth. Sci.* 11, 1241975. <https://doi.org/10.3389/feart.2023.1241975>.
- [31]. Rogers, J.J.W., & Greenberg, J.K. (1990). Late-Orogenic and Anorogenic granites: Distribution by major elements and trace elements chemistry and possible origins. *J. Geol.* 98, 291-309.
- [32]. Ramadan, T.M., Ibrahim, T.M., Said, A., & Bayoumi, M.B. (2013). Application of remote sensing in exploration for uranium mineralization in Gabal El Sela area, south Eastern Desert, Egypt. *J. Remote Sens. Space. Sci.* 16:199–210

- [33]. Abdel Gawad, A.E., Orabi, A.H., & Bayoumi, M.B. (2015). Uranium evaluation and its recovery from microgranite dike at G. El Sela area, South Eastern Desert, Egypt. *Arab. J. Geosci.* 8, 4565–4580. <https://doi.org/10.1007/s12517-014-1499-3>
- [34]. Frost, B.R., Barnes, C.G., Collins, W.J., Arculus, R.J., Ellis, D.J., & Frost, C.D. (2001). A geochemical classification for granitic rocks. *J. Petrol.* 42 (11), 2033–2048. <https://doi.org/10.1093/petrology/42.11.2033>.
- [35]. El-Feky, M.G., El Mowafy, A.A., & Abdel Warith, A. (2011). Mineralogy, geochemistry, radioactivity and environmental impacts of Gabal Marwa granites, southeastern Sinai, Egypt. *Chin. J. Geochem.* 30, 175–186. <https://doi.org/10.1007/s11631-011-0499-1>.
- [36]. Gaafer, I., Cuney, M., & Abdel Gawad, A.E. (2014). Mineral chemistry of two-mica granite rare metals: impact of geophysics on the distribution of uranium mineralization at El Sela shear zone, Egypt. *Open J. Geol.* 4:137–160. [doi:10.4236/ojg.2014.44011](https://doi.org/10.4236/ojg.2014.44011)
- [37]. Lee, S.G., Asahara, Y., Tanaka, T., Kim, N.H., Kim, K.H., Yi, K., Masuda, A., & Song, Y.S. (2010). La–Ce and Sm–Nd isotopic systematics of early Proterozoic leucogranite with tetrad REE pattern. *Chem. Geol.* 276, 360–373. <https://doi.org/10.1016/j.chemgeo.2010.07.003>.
- [38]. Saad, A.M., Sakr, M.A.H., Selim, M.S.A. et al. Geotechnical and geophysical investigations for infrastructure safety zones: a case study of the supporting ring road, Cairo, Egypt. *Sci Rep* 14, 29670 (2024). <https://doi.org/10.1038/s41598-024-72337-8>
- [39]. Anjos, R.M., Veiga, R., Soares, T., Santos, A.M.A., Aguiar, J.G., Frasca, M.H.B.O., Brage, J.A.P., Uzeˆda, D., Mangia, L., Facure, A., Mosquera, B., Carvalho, C., & Gomes, P.R.S. (2005). Natural radionuclide distribution in Brazilian commercial granites. *Radiat. Meas.* 39, 245–253. <https://doi.org/10.1016/j.radmeas.2004.05.002>.
- [40]. El Nahas, H.A., El Feky, M.G., & Mira, H. (2011). Mineralogy, M-type tetrad effect and radioactivity of altered granites at the G. Abu Garadi shear zone, Central Eastern Desert, Egypt. *Chin. J. Geochem.* 30, 153–164. <https://doi.org/10.1007/s11631-011-0497-3>.
- [41]. El Aassy, I.E., El Galy, M.M., Nada, A.A., El Feky, M.G., Abd El Maksoud, T.M., Talaat SM, & Ibrahim, E.M. (2011). Effect of alteration processes on the distribution of radionuclides in uraniumiferous sedimentary rocks and their environmental impact, southwestern Sinai, Egypt. *J. Radioanal. Nucl. Chem.* 289:173–184
- [42]. Abu Hassan, S.E., Ibrahim, E.M., El Aassy, I.E., & Abd El Maksoud T.M. (2022). Uranium fingerprint for some sedimentary rock samples, Southwestern Sinai, Egypt, *J. Appl. Phys.* 14, 1–10.
- [43]. Ekwere, S.J. (1985). Li, F and Rb contents and Ba/Rb and Rb/Sr ratios as indicators of post-magmatic alteration and mineralization in the granitic rocks of the Banke and Ririwai younger granite complexes, North Nigeria. *Mineral. Deposita* 20, 89–93. <https://doi.org/10.1007/BF00204315>.
- [44]. Anders, E., & Grevesse, N. (1989). The Abundances of the Elements: Meteoritic and Solar. *Geochimica et Cosmochimica Acta*, 53, 197-214. [https://doi.org/10.1016/0016-7037\(89\)90286-X](https://doi.org/10.1016/0016-7037(89)90286-X).
- [45]. Erlank, A.J., Marchant, J.W., Cardoso, M.P., & Ahrens, L.H. (1978). Zirconium. In: Wedepohl, K.H., Ed., *Handbook of Geochemistry*, Vol. 11/4, Springer, Berlin, 40.
- [46]. Fawzy, K.M. (2017). Characterization of a Post Orogenic A-Type Granite, Gabal El Atawi, Central Eastern Desert, Egypt: Geochemical and Radioactive Perspectives. *Open Journal of Geology*, 7, 93-117. <http://www.scirp.org/journal/ojg>.
- [47]. Visser, J.N.J., & Young, G.M., (1990). Major element geochemistry and paleoclimatology of the Permo-Carboniferous glaciogene Dwyka Formation and post-glacial mudrocks in southern Africa. *Palaeogeography, Palaeoclimatol. Palaeoecol.* 49, 57–81. [http://doi.org/10.1016/0031-0182\(90\)90039-A](http://doi.org/10.1016/0031-0182(90)90039-A).
- [48]. Odigi, M.I., & Amajor, L.C. (2009). Geochemical characterization of Cretaceous sandstones from the Southern Benue Trough, Nigeria. *Chin. J. Geochem.* 28, 44–54. <http://doi.org/10.1007/s11631-009-0044-7>.
- [49]. Gascoyne, M., Miller, N.H., & Neymark, L.A. (2002). Uranium-series disequilibrium in tuffs from Yucca Mountain, Nevada, as evidence of pore-fluid flow over the last million years. *Appl. Geochem.* 17(6), 781–92. [https://doi.org/10.1016/S0883-2927\(02\)00038-0](https://doi.org/10.1016/S0883-2927(02)00038-0).
- [50]. Pękala, M., Kramers, J.D., & Waber, H.N., (2010). $^{234}\text{U}/^{238}\text{U}$ activity ratio disequilibrium technique for studying uranium mobility in the Opalinus Clay at Mont Terri, Switzerland. *Applied Radiation and Isotopes*, 68, 984–992. <https://doi.org/10.1016/j.apradiso.2010.02.009>.
- [51]. Taalab, S.A., Hanfi, M.Y., Ahmed, M.S., Saadawi, D.A., Sakr, A.K., Khandaker, M.U., & Khattab, M.R. (2024b). Geochemical evaluation and hazard indices due to radioactive minerals associated with granitic areas, *Nuclear Engineering and Technology*, 56, 11,4921-4928. <https://doi.org/10.1016/j.net.2024.08.027>.
- [52]. Brennecke, G.A., Weyer, S., Wadhwa, M., Janney, J.P., EZipfel, J., & Anbar, A.D. (2010). $^{238}\text{U}/^{235}\text{U}$ Variations in Meteorites: Extant 247 Cm and Implications for Pb-Pb Dating. *Science*. 327 (5964), 449-51. <https://doi.org/10.1126/science.1180871>.
- [53]. Dawood, Y.H. (2001). Uranium-series disequilibrium dating of secondary uranium ore from the south Eastern Desert of Egypt, *Appl. Radiat. Isot.* 55, 881–887. <https://doi.org/10.1007/s11631-011-0499-1>.
- [54]. El Aassy, I.E., El Galy, M.M., Nada, A.A. et al. (2011). Effect of alteration processes on the distribution of radionuclides in uraniumiferous sedimentary rocks and their environmental impact, southwestern Sinai, Egypt. *J. Radioanal. Nucl. Chem.* 289, 173–184. <https://doi.org/10.1007/s10967-011-1059-1>.

- [55]. Miallier, D., Condomines, M., Pilleyre, T., Sanzelle, S., Guittet, J. (2004). Concordant thermoluminescence and ^{238}U – ^{230}Th ages for a trachytic dome (Grand Sarcoui) from the Chaîne des Puys (French Massif Central). *Quaternary Science Reviews*, 23, 709-715. <https://doi.org/10.1016/j.quascirev.2003.06.002>.
- [56]. [56] Thiel, K., Vorwerk, R., Saager, R., & Stupp, H.D. (1983). ^{235}U fission tracks and ^{238}U -series disequilibria as a means to study recent mobilization of uranium in Archaean pyritic conglomerates. *Earth Planet. Sci. Lett.* 65(2), 249-262. [https://doi.10.1016/0012-821X\(83\)90164-4](https://doi.10.1016/0012-821X(83)90164-4).
- [57]. Noseck, U.T., Brasser, J., Suksi, V., Havlova, M., Hercik, M.A., Denecke, H.J., Forster, (2008). Identification of uranium, enrichment scenarios by multi-method characterisation of immobile uranium phases, *Phys. Chem. Earth* 33, 969–977.
- [58]. Stohl, F.V., & Smith, D.K. (1981). *The Crystal Chemistry of the Uranyl Silicate Minerals [M]*. Department of Geosciences, the Pennsylvania State University, University Park. Pennsylvania.
- [59]. Taalab, S.A, Abdel-Rahman, A.M., El-Awny, H., Awad, H.A., Zakaly, H.M.H., Fahmy, W., Ene, A. (2023a). Petrogenesis and Tectonic Evolution of Kab Amiri Ophiolites and Island-Arc Assemblages, Central Eastern Desert, Egypt: Petrological and Geochemical Constraints. *Minerals* 13, 528. <https://doi.org/10.3390/min13040528>
- [60]. Raslan, M.F., El-Shall, H.E., Omar, S.A., & Daher, A.M. (2010a). Mineralogy of polymetallic mineralized pegmatite of Ras Baroud granite, Central Eastern Desert, Egypt. *J. of Mineral. and Petrol. Sci.* 105, 123-134. <https://doi.10.2465/jmps.090201>.
- [61]. El Aassy, I.E. M.M. El Galy, A.A. Nada, M.G. El Feky, T.M. Abd El Maksoud, S.M. Talaat and E.M. Ibrahim, J. *Radioanal. Nucl. Chem.* 289(1), 173–84 (2011).
- [62]. Assaf HS, Mahdy MA, El Afandy A (1997) Egyptian younger granites: an approach to define parameters favoring formation of uranium deposits. In: 3rd conference of geochemistry, Alexandria, 3–4 Sept 1997, pp 409–420.